PICTURE OF THE MONTH

Multilevel Cloud Structures over Svalbard

ANDREAS DÖRNBRACK AND SONJA GISINGER

Institut für Physik der Atmosphäre, DLR Oberpfaffenhofen, Wessling, Germany

MICHAEL C. PITTS

NASA Langley Research Center, Hampton, Virginia

LAMONT R. POOLE

Science Systems and Applications, Inc., Hampton, Virginia

MARION MATURILLI

Alfred Wegener Institute, Helmholtz Centre for Polar and Marine Research, Potsdam, Germany

(Manuscript received 7 June 2016, in final form 3 November 2016)

ABSTRACT

The presented picture of the month is a superposition of spaceborne lidar observations and high-resolution temperature fields of the ECMWF Integrated Forecast System (IFS). It displays complex tropospheric and stratospheric clouds in the Arctic winter of 2015/16. Near the end of December 2015, the unusual northeastward propagation of warm and humid subtropical air masses as far north as 80°N lifted the tropopause by more than 3 km in 24 h and cooled the stratosphere on a large scale. A widespread formation of thick cirrus clouds near the tropopause and of synoptic-scale polar stratospheric clouds (PSCs) occurred as the temperature dropped below the thresholds for the existence of cloud particles. Additionally, mountain waves were excited by the strong flow at the western edge of the ridge across Svalbard, leading to the formation of mesoscale ice PSCs. The most recent IFS cycle using a horizontal resolution of 8 km globally reproduces the large-scale and mesoscale flow features and leads to a remarkable agreement with the wave structure revealed by the spaceborne observations.

1. Introduction

The ''picture of the month'' as presented in this short contribution is not a photo of the sky spontaneously shot from a digital camera. The picture as displayed in Fig. 1 is a combination of spaceborne measurements by the Cloud–Aerosol Lidar with Orthogonal Polarization (CALIOP) instrument on board the *Cloud–Aerosol Lidar and Infrared Pathfinder Satellite Observations* (*CALIPSO*) satellite during one of several Arctic overpasses on 30 December 2015 and a high-resolution short-term forecast of a numerical weather prediction (NWP) model utilizing an unprecedented global resolution of about 8 km (for data sources, see the appendix). In our days of ceaseless swells of pictures taken everywhere and anytime on the planet, a snapshot taken from a sensor much different than a camera, taken from a perspective so much different than from Earth, and superimposed with numerical predictions reflecting the observed flow features with a remarkable realism elicits wonder and admiration.

The selected picture of the month displays tropospheric and stratospheric cloud structures that appeared simultaneously during a remarkable meteorological situation in the high Arctic near Svalbard on 30 December 2015. The resulting spectacular and uncommon appearance of diverse cloud types and structures at different layers reaching up to 28-km altitude was documented by the CALIOP measurements of total

Corresponding author e-mail: Andreas Dörnbrack, andreas.doernbrack@dlr.de

DOI: 10.1175/MWR-D-16-0214.1

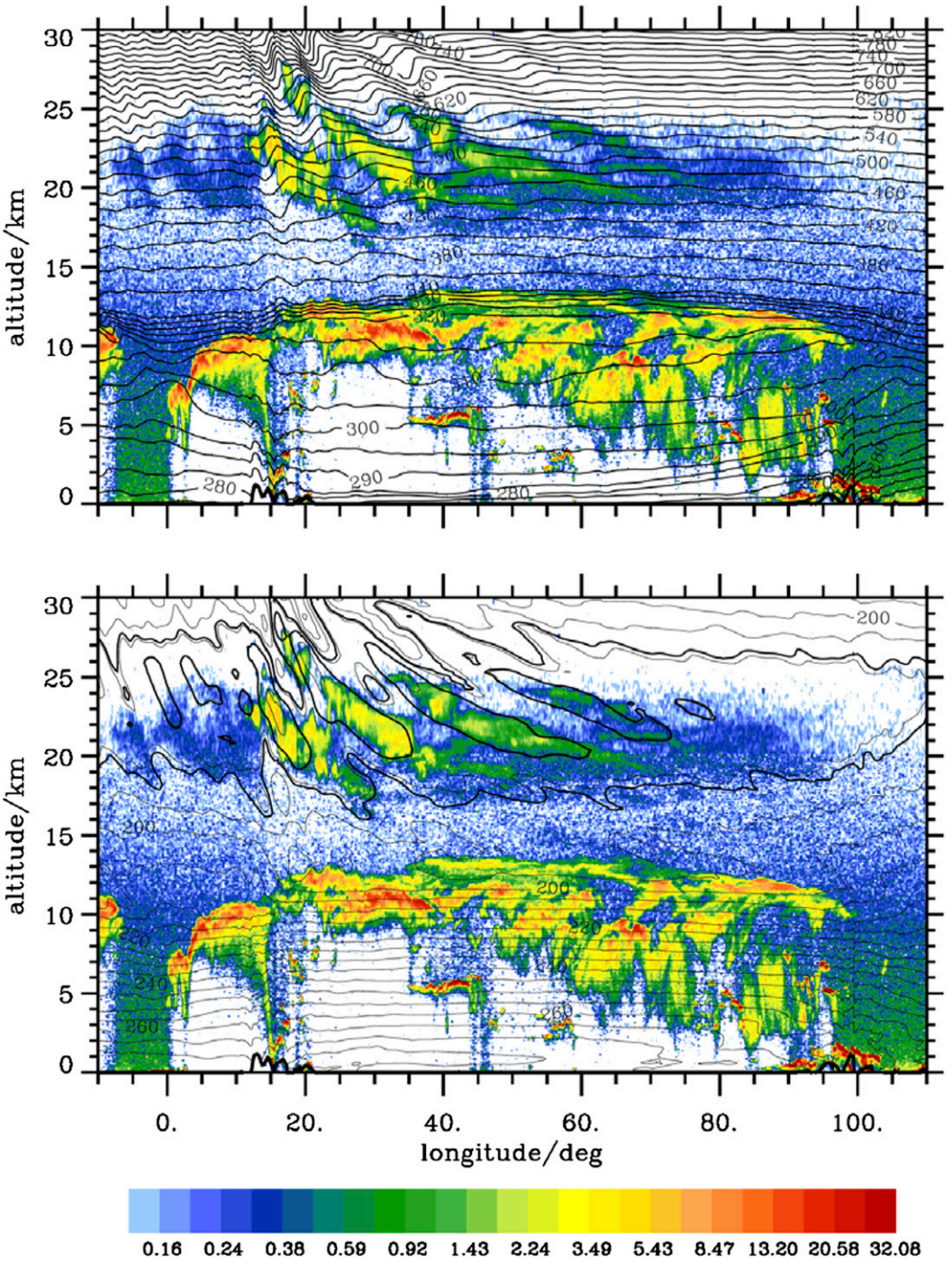

FIG. 1. Composite of 532-nm total attenuated backscatter (10^{-3} km^{-1} sr^{-1}, color shaded) from CALIOP and ECMWF (top) potential temperature (K, solid black lines) and (bottom) absolute temperature (K, thin black lines every 5 K and thick black lines at 185 and 191 K) valid at 0400 UTC 30 Dec 2015 (+4-h lead time from the 0000 UTC HRES IFS forecast of cycle 41r2).

attenuated backscatter at 532 nm (Fig. 1a). The CALIOP observations show an extensive, elongated structure of cirrus clouds within the upper troposphere up to an altitude of about 13 km. The cirrus clouds are also nicely seen in the infrared satellite image at this time (Fig. 2). Slightly more than 6 km above this cirrus deck, CALIOP detected a nearly 8-km-deep layer of synoptic-scale polar stratospheric clouds (PSCs) embedded in an

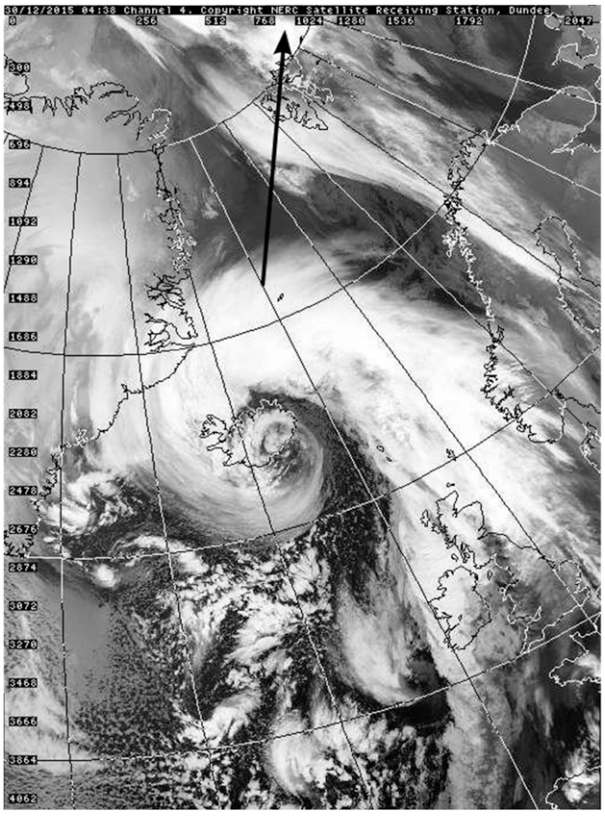

FIG. 2. Thermal infrared image (*NOAA-19*, channel 4: 10.3–11.3 μm) at 0440 UTC 30 Dec 2015 with the first third of the path of the CALIOP measurements (Fig. 1) indicated by a black arrow. Image provided by NERC Satellite Receiving Station, Dundee University, Scotland (http://www.sat.dundee.ac.uk).

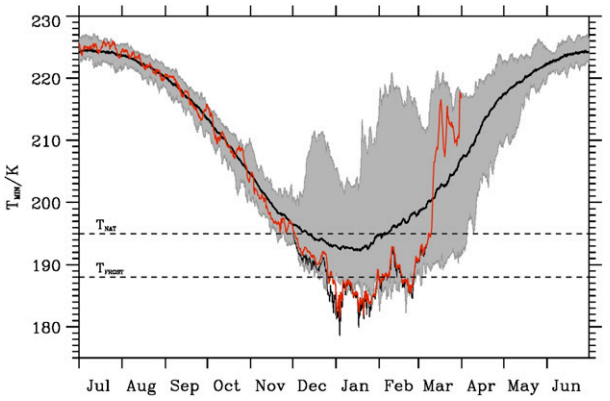

FIG. 3. The 6-hourly ECMWF interim reanalysis (ERA-Interim; Dee et al. 2011) data retrieved at a horizontal resolution of 1°: minimum temperature T_{MIN} (K) between 65° and 90°N at the 50-hPa pressure surface. The thick black line denotes the mean values of T_{MIN} averaged during 1979–2015, and the shaded areas encompass the minimum and maximum values of T_{MIN} attained at every date between 1979 and 2015. The red line marks the evolution of T_{MIN} from operational analyses of the IFS cycle 41r1 until 8 Mar 2016. The thin black line indicates T_{MIN} from the IFS cycle 41r2 in the preoperational phase 1 Dec 2015–8 Mar 2016 retrieved at a resolution of 0.125°. After 8 Mar 2016, the black line continues as red curve of the operational IFS cycle 41r2.

extended cold layer with temperatures less than 191 K. Within this layer, vertically tilted and horizontally separated patterns of enhanced attenuated backscatter are collocated with cold stratospheric temperature values less than 185 K (Fig. 1b). They are reminiscent of mountain-wave-induced PSCs (e.g., Maturilli and Dörnbrack 2006, their Fig. 9). This first, qualitative interpretation is supported by the very structured ice PSCs occurring in a region both above and downstream of Svalbard's mountains and above the underlying clouds near the tropopause as mentioned above. As shown later, the satellite trace (as sketched in Figs. 3 and 6) was nearly parallel to the stratospheric winds at this time and the mountain-wave-induced temperature anomalies are tilted into the ambient wind.

The spectacular display of PSCs[1] has fascinated people for a long time and they have been observed scientifically since the 1880s (e.g., Backhouse 1885; Geelmuyden 1885; Mohn 1893; Stanford and Davies 1974). A first step to explain the nature of these clouds was the exact determination of their height range between 20 and 30 km by Störmer (1929, 1931). During the recent 30 years, PSCs were systematically monitored because chemical reactions on cloud particles play a major part in the depletion of the ozone layer (Solomon 1999). The reactions are very efficient at low temperatures due to the increase in particle surface area and in heterogeneous reaction rates (Peter 1997). The large interannual variability of the Arctic polar vortex and of the polar cap minimum temperatures attained during Northern Hemispheric winters (Fig. 3) regularly sparks off the scientific interest about the possible formation of PSCs and the consequential ozone depletion in spring. For an overview of the evolution of the recent winter 2015/16, see the excellent review by Manney and Lawrence (2016).

PSCs form in a variety of ways. First of all, the ambient stratospheric temperatures must fall below a certain threshold where liquid or solid particles can form. Here, different freezing processes (homogeneous and/or heterogeneous freezing) determine the composition of the PSC particles. Generally, one differentiates between ice PSCs, which can exist at $T < T_{FROST}$, solid nitric acid trihydrate (NAT) PSCs, which can exist at $T < T_{NAT}$ ($\approx T_{FROST} + 7$ K), and liquid supercooled ternary solution (STS; $HNO_3/H_2O/H_2SO_4$) PSCs, which can exist at $T \lesssim T_{FROST} + 3$ K. Since T_{FROST} depends on

[1] These clouds are often called mother-of-pearl clouds because of their magnificent display of spectral colors.

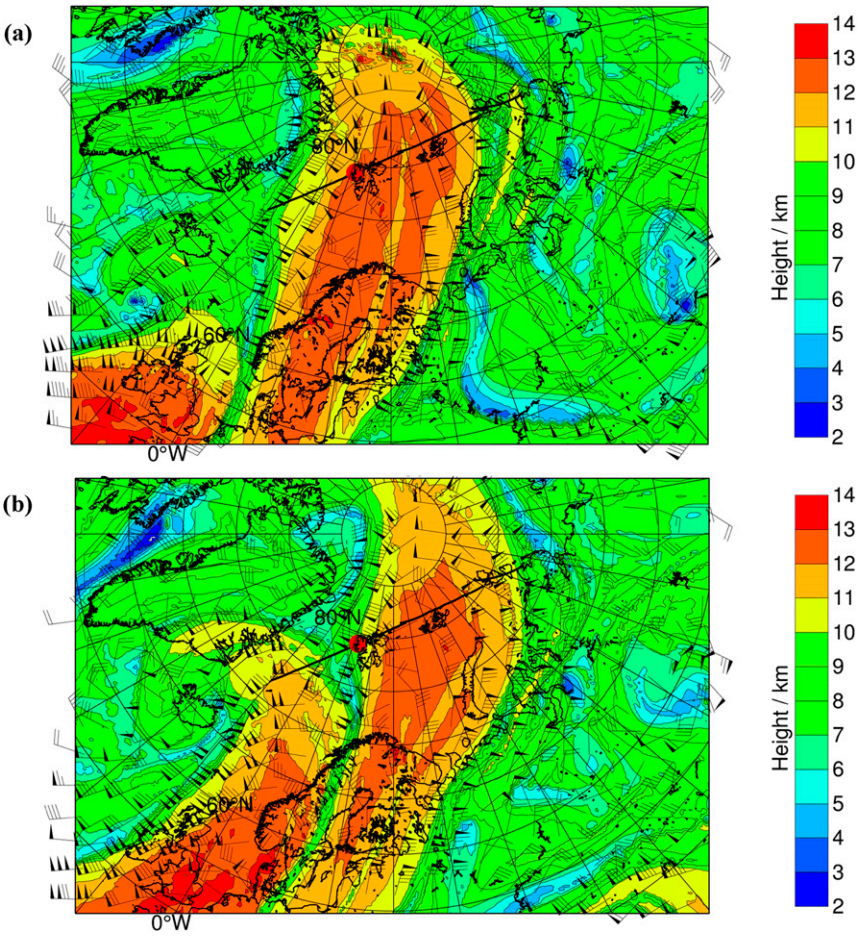

FIG. 4. Height of the dynamical tropopause (km, color shaded) and horizontal wind (m s^{-1}, barbs) at the 2-PVU surface at (a) 1800 UTC 29 Dec 2015 and (b) 0600 UTC 30 Dec 2015. The path of the *CALIPSO* overpass is plotted as a solid black line, and the location of Ny-Ålesund, Svalbard, is marked by a red dot.

atmospheric humidity it varies with altitude ($T_{FROST} \approx$ 188 K at 50 hPa and $T_{FROST} \approx$ 185 K at 30 hPa). PSCs can be observed in situ by instruments flying on balloons (e.g., Rosen et al. 1992) or by in situ airborne sensors (e.g., Dye et al. 1996). The high altitudes and vertical extent of PSCs favor remote sensing systems such as lidars operated on the ground (e.g., Di Liberto et al. 2014) or on an aircraft (e.g., Browell et al. 1990), or satellite solar occultation PSC measurements (e.g., Strawa et al. 2002). Most of the recent studies on PSCs focused on the composition and sizes of the particles (e.g., Reichardt et al. 2015) and chemical processes occurring at their surfaces that yield ozone-destructive, reactive chlorine species (e.g., Solomon 1999).

Numerical modeling of PSCs has always been a challenging task as chemical and dynamical aspects of their formation and existence must be combined (e.g., Reichardt et al. 2004). Their formation is primarily influenced by large-scale processes such as the radiative cooling inside the Arctic polar vortex. Moreover, it is known that both synoptic scale as well as mesoscale weather systems influence the formation of PSCs and the associated chemical reactions (Teitelbaum and Sadourny 1998; Carslaw et al. 1998). Simulation of mesoscale mountain waves especially posed a challenge, and special methods such as linear wave prediction models and mesoscale forecast models were used in the past to predict their local formation (e.g., Dörnbrack et al. 1998; Eckermann et al. 2006). In this day and age, global operational NWP models use spatial resolutions, which hardly could be attained by limited-area models several years ago. For example, the European Centre for Medium-Range Weather Forecasts (ECMWF) currently runs its operational predictions of the Integrated Forecast System (IFS) cycle 41r2 at 8 km globally (Hólm et al. 2016; Malardel and Wedi 2016). Here, it will be shown that the conditions under which the observed mesoscale ice PSCs formed can be resolved by the IFS.

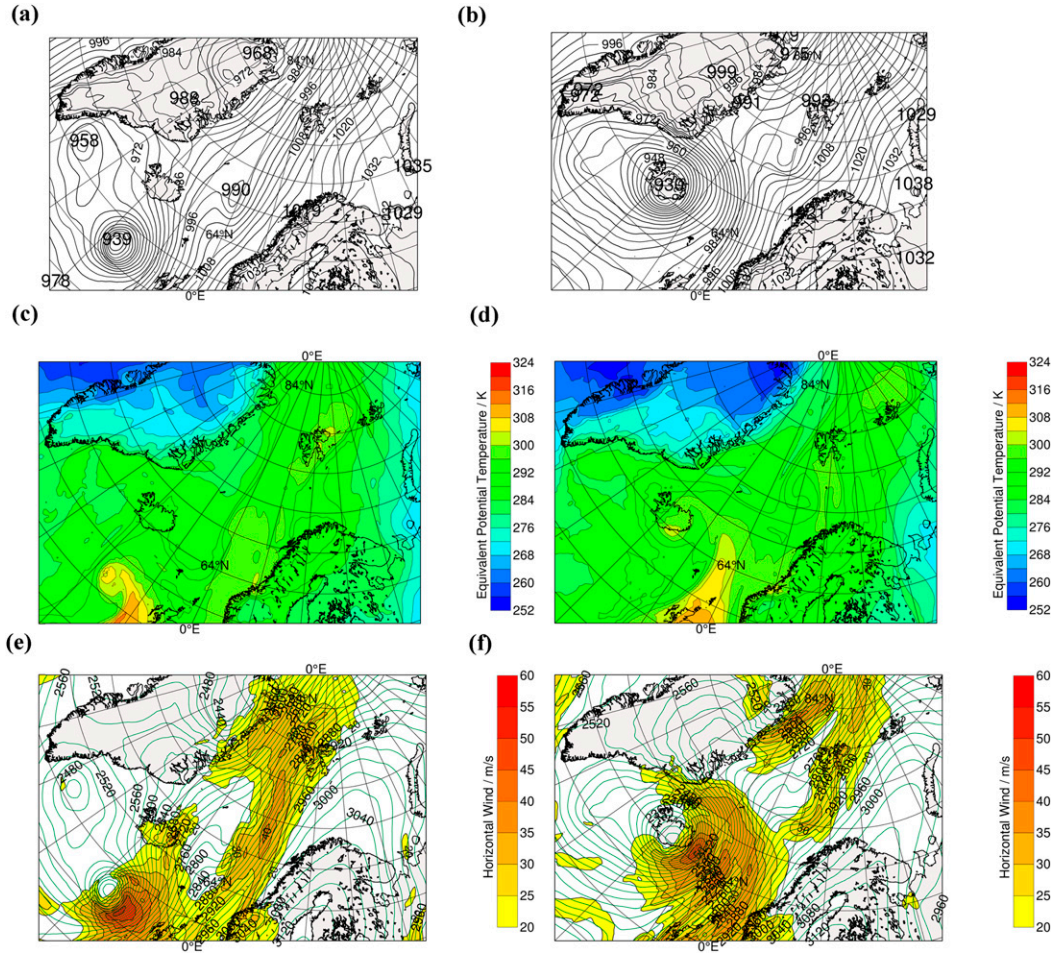

FIG. 5. Tropospheric charts valid at (left) 1800 UTC 29 Dec 2015 and (right) 0600 UTC 30 Dec 2015. (a),(b) Mean sea level pressure (hPa, contour lines); (c),(d) equivalent potential temperature (K, color shaded) at 850 hPa; and (e),(f) horizontal wind ($m\,s^{-1}$, color shaded) and geopotential height (m, contour lines) at 700 hPa.

2. Weather situation and gravity wave characteristics

a. *Cold Arctic polar vortex*

The composite picture of the month was taken in a period when the temperatures inside the Arctic stratospheric vortex were unusually cold (Fig. 3). In November–December 2015, the Arctic vortex was minimally disturbed by upward-propagating planetary waves (Matthias et al. 2016) and the polar cap minimum temperature T_{MIN} between 65° and 90°N dropped well below the climatological mean. The red T_{MIN} line in Fig. 3 reveals that the threshold of T_{NAT} at 50 hPa was already reached at the beginning of December 2015, and T_{MIN} dropped below T_{FROST} at the end of 2015. Apparently, the minimum temperatures falling below T_{FROST} at the end of the year constitute a new record. In its further evolution, the Arctic polar vortex remained cold, stable, and coherent until the end of February 2016 (Manney and Lawrence 2016). The final warming already occurred at the beginning of March 2016. Such an early collapse of the cold polar vortex is in accordance with the findings of the climatological study of Hu et al. (2014). In such a cold stratospheric environment, the period of temperatures below T_{FROST} and T_{NAT} at 50 hPa lasted more than one month and three months, respectively. *CALIPSO* observations until the end of January 2016 confirm the widespread occurrence of PSCs in the Arctic.

b. *Tropospheric flow conditions*

Near the end of December 2015, the tropospheric flow over the northern Atlantic was characterized by an anticyclonic Rossby wave breaking event. Figure 4 illustrates the late stages of this event by means of the height and wind at the 2-PVU (1 PVU = $10^{-6}\,K\,kg^{-1}\,m^2\,s^{-1}$) surface from the ECMWF operational analyses valid at 1800 UTC 29 December 2015 and 12 hours later at 0600 UTC

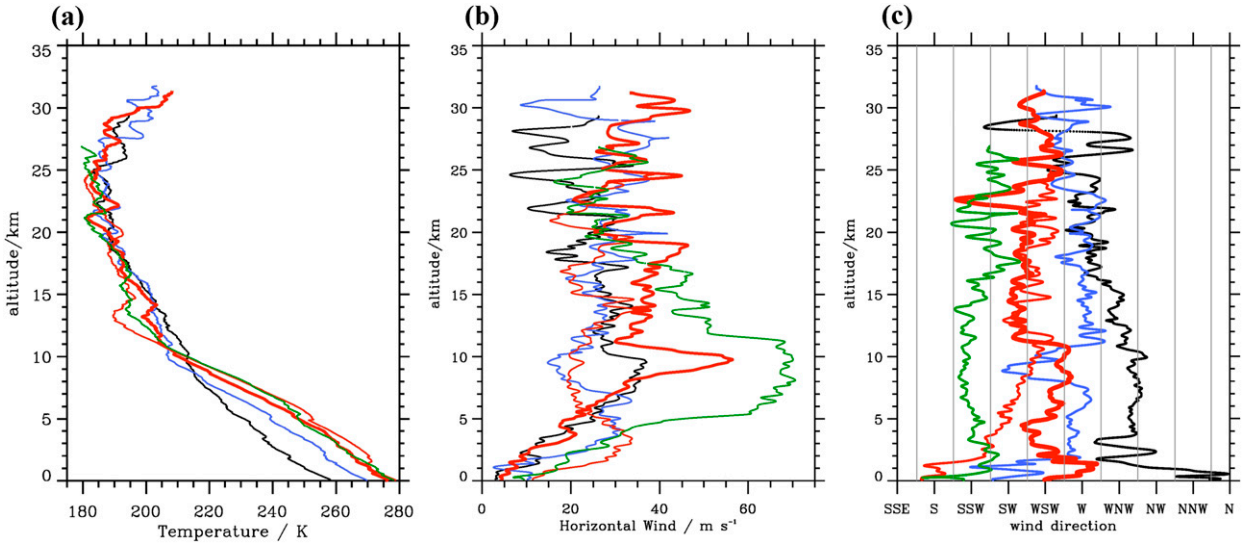

FIG. 6. Vertical profiles of (a) absolute temperature, (b) horizontal wind, and (c) wind direction from radiosonde launches in Ny-Ålesund, Svalbard, at 1200 UTC 27 Dec (black), 1200 UTC 28 Dec (blue), 1200 UTC 29 Dec (thin red), 1200 UTC 30 Dec (thick red), and 1200 UTC 31 Dec (green) 2015.

30 December 2015, respectively. A ridge with tropopause heights of up to 13 km extended north to latitudes above 80°N. Between this ridge with high surface pressure (maximum at about 1038 hPa) over eastern Europe and a surface pressure low over Greenland (minimum at about 968 hPa), a strong southwesterly low-level flow extended over the entire northern Atlantic and the Norwegian Sea toward Svalbard (Figs. 5a,b). East of Greenland, warm and moist air was advected northward as shown by the increased values of the equivalent potential temperature (Figs. 5c,d). Farther south near Iceland, a storm with a core pressure of 930 hPa at 0600 UTC 30 December 2015 propagated north. This weather situation led to a combination of two processes relevant for the cloud structures as shown in Fig. 1. First, the increase of the tropopause height associated with the anticyclonic Rossby wave breaking led to a cooling of the air masses in the upper troposphere–lower stratosphere (UTLS) due to adiabatic expansion. Second, the strong troposphere-deep pressure gradient between the upstream Greenland–Iceland cyclone complex and the downstream Scandinavian ridge forced a strong flow across the mountains of Svalbard, which reached a maximum at 0000 UTC 30 December 2015 with horizontal winds larger 25 m s^{-1} at 700 hPa (Figs. 5e,f).

A series of five radiosonde ascents from Ny-Ålesund, Svalbard (79°N, 12°E), covering the period from 27 to 31 December 2015 (Fig. 6) illustrates the previous findings from the IFS analyses. First of all, the warming of the troposphere by about 15 K due to the warm-air advection can be clearly seen in Fig. 6a. During the same period, the tropopause rose and sharpened dramatically. Indeed, the vertical temperature profiles at 1200 UTC 29 and 30 December 2015 are more typical for a midlatitude station than for an Arctic location.

c. *Large-scale cooling*

An analysis of radiosonde soundings from Ny-Ålesund, Svalbard, reveals a drop of the mean temperature between 10 and 13 km by about 9 K in 3 days reaching 200 K on 29 December (see Table 1). This strong cooling associated with the tropopause ascent led to the formation of the observed cirrus clouds at these levels. Not only did the temperature in the vicinity of the tropopause drop, but the mean stratospheric temperature between 20- and 25-km altitude also decreased by about 4 K due to the lifting of the atmosphere above the ridge (Table 1). In this way, the mean temperatures near 30 hPa dropped below 185 K, the ice existence temperature T_{FROST}. However,

TABLE 1. Mean quantities in the UTLS averaged from 10- to 13-km altitude: absolute temperature T^{TP}, horizontal wind V_H^{TP}, and wind direction α^{TP} from the radiosonde soundings in Ny-Ålesund. The mean stratospheric temperature T^{SP} is averaged from 20- to 25-km altitude and ΔT^{SP} is the difference between the measured maximum and minimum T in this layer.

Date (2015)	T^{TP} (K)	V_H^{TP} (m s^{-1})	α^{TP} (K)	T^{SP} (K)	ΔT^{SP} (K)
26 Dec	209.3	8.7	254	188.8	4.7
27 Dec	209.6	27.7	296	187.4	6.5
28 Dec	205.9	23.3	268	187.3	8.4
29 Dec	200.0	23.6	240	184.4	12.0
30 Dec	204.7	36.8	241	185.4	10.1
31 Dec	204.1	59.8	199	183.9	6.8

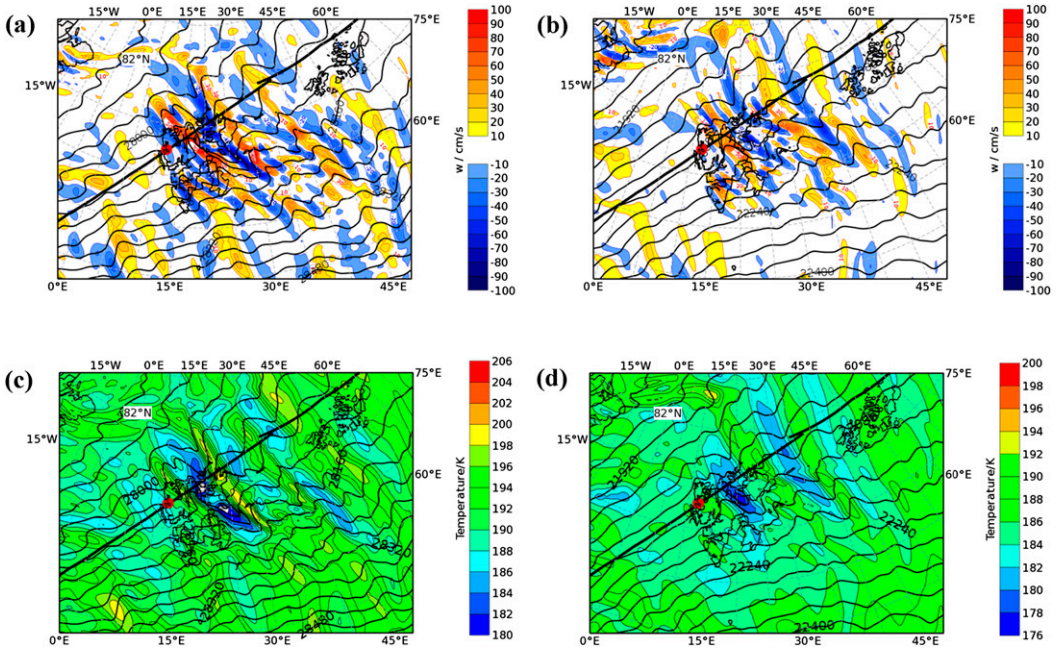

FIG. 7. (a),(b) Vertical velocity (m s^{-1}, color shading) and (c),(d) absolute temperature (K, color shading) and geopotential height (m, black contour lines) from the IFS cycle 41r2 at (left) 10 and (right) 30 hPa valid at 0600 UTC 30 Dec 2015. The path of the *CALIPSO* overpass is plotted as solid black line, and the location of Ny-Ålesund, Svalbard, is marked by a red dot.

increased backscatter values indicative of ice PSCs appear primarily at and leeward of the wave crests as shown in Fig. 1a. The adiabatic cooling by ascending air parcels led to a local temperature decrease and to ice nucleation, which require temperatures $T \lesssim T_{\mathrm{FROST}} - 4\,\mathrm{K}$. Thus, we conclude that the stratospheric ice clouds as seen by CALIOP were generated due to mountain-wave-induced temperature anomalies.

d. Mountain-wave-induced cooling

As documented in Table 1, the magnitude of stratospheric temperature fluctuations ΔT^{SP} measured in the layer from 20 to 25 km increased from values of around 5 K on 26 December 2015 to values up to 12 K on 29 and 30 December 2015. These fluctuations are represented by the wavelike temperature perturbations as shown in Fig. 1b. There, the areas of increased backscatter nearly coincide with localized regions of $T < T_{\mathrm{FROST}}$. It must be noted that the *CALIPSO* satellite trace was nearly aligned with the stratospheric winds as indicated by the orientation of the contour lines of the geopotential height in Fig. 7. Therefore, the ice PSCs, as well as the simulated mountain waves, are tilted into the ambient stratospheric wind, which is oriented from west to east in Fig. 1. The tilting into the ambient wind is characteristic for upward-propagating mountain waves (Nappo 2012).

Figure 7 depicts horizontal cross sections of the stratospheric wave structure at 10 and 30 hPa by means of the vertical velocity and the absolute temperature from IFS analyses. A sequence of northwest–southeast-oriented updraft–downdraft couplets extends from Svalbard toward the northeast. Altogether, there are four stratospheric cold anomalies associated with the adiabatic cooling in the mountain waves at 10 hPa (Figs. 7a,c). Their positions clearly correspond to the areas of $T < 185\,\mathrm{K}$ and the CALIOP PSC observations as presented in Fig. 1b. At the lower level of 30 hPa (Figs. 7b,d), similarly oriented structures exist whereby the cold areas are slightly shifted to the northeast in accordance with the tilt of the observed PSCs (Fig. 1).

e. Gravity wave characteristics

Mountain waves are generated and propagate into the stratosphere if there is a major flow across the topography (low-level forcing), the tropospheric and stratospheric winds are large enough to avoid the formation of wave-induced critical levels, and there is no significant turning of the wind with altitude (e.g., Fritts et al. 2016). All these requirements were satisfied in the Svalbard region for the period from 28 to 30 December 2015. The horizontal wind in the lower troposphere (averaged from 2- to 5-km altitude) increased gradually from about 5 to about 30 m s^{-1} in the period from 25 to 31 December 2015 as shown by the radiosonde data (Fig. 8a). Also near the tropopause level, the averaged wind in the UTLS increased markedly after 28 December up to

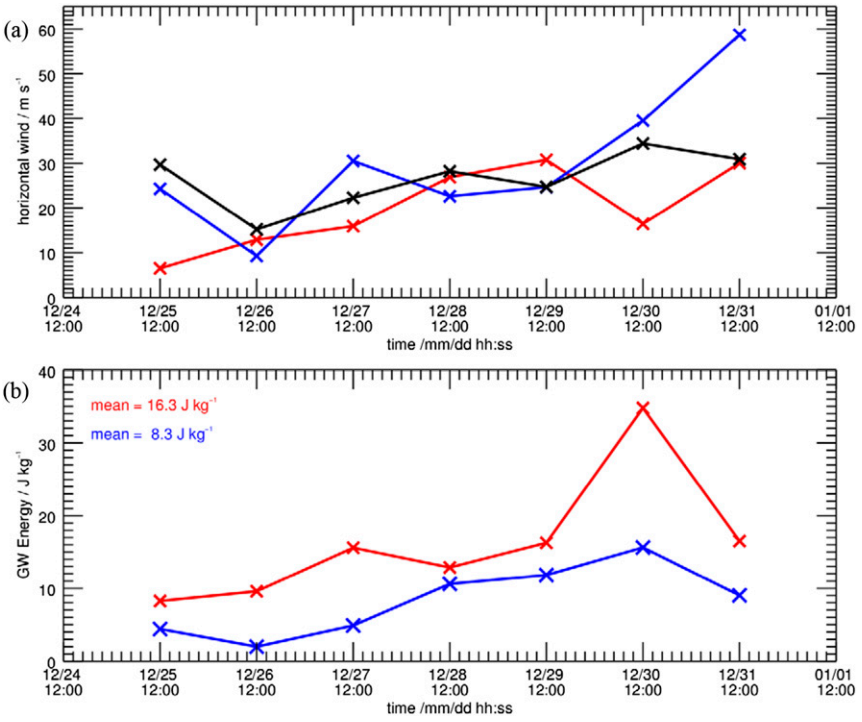

FIG. 8. (a) Vertically averaged horizontal wind in the lower troposphere (2–5 km, red crosses), the tropopause region (8–15 km, blue crosses), and in the stratosphere (15–25 km, black crosses). (b) Stratospheric gravity wave kinetic and potential energies (red and blue crosses, respectively) determined from the radiosonde soundings of Ny-Ålesund, Svalbard, in an altitude range of 15–25 km.

values of 60 m s^{-1} and turned from westerly to southwesterly as the ridge propagated over Svalbard (Table 1). Altogether, the directional shear between tropospheric and stratospheric winds weakened in this period (Fig. 6c). The combination of strong winds in the lower troposphere followed by increased mid- to upper-tropospheric winds and the presence of wind of about 25 m s^{-1} in altitudes above (15–25 km) created a favorable flow situation for mountain wave excitation and vertical propagation to higher altitudes. Indeed, both the temperature and wind profiles from the radiosonde soundings reveal wavelike structures in the stratosphere (Fig. 6) that were analyzed to estimate the kinetic and potential energies of the gravity waves as well as their intrinsic frequency and horizontal wavelength from the radiosonde soundings.

For this purpose, a polynomial fit was applied to calculate background profiles of the horizontal wind components and the potential temperature from the radiosonde profiles between 15- and 25-km altitude. The perturbations calculated as the difference between the background profiles and the actual radiosonde profiles were treated as signatures of internal gravity waves from which the kinetic and potential energies are determined according to Murphy et al. (2014). Figure 8b shows a peak in the stratospheric kinetic and potential energy densities at 30 December 2015. This enhancement as well as the localized wave appearance over and in the lee of Svalbard (Fig. 7) indicates that the waves are generated by the flow over the mountains. Stokes's analysis of the velocity perturbations (Eckermann and Vincent 1989) of the 30 December radio sounding revealed the intrinsic frequency Ω of the dominant gravity wave mode being 6.7f, where f is the Coriolis parameter. Assuming that the dominant gravity wave mode is a stationary mountain wave its horizontal wavelength can be calculated using the relationship between Ω, horizontal wavenumber k, and the background wind U for stationary waves $\Omega = -kU$ (i.e., Nappo 2012). Having a background wind of 25–35 m s^{-1} (Fig. 8a), the determined horizontal wavelength is approximately 180, . . . , 250 km. The effect of the Coriolis force alters the dispersion relationship of nonrotating hydrostatic gravity waves and allows a slantwise (e.g., horizontal and vertical) propagation (Gill 1982, chapter 8). This explains the multiple mountain-wave-induced temperature anomalies separated by about 180 km (Figs. 1b and 7d). Another example of a similar stratospheric cloud structure above Scandinavia and a more detailed discussion can be found in Dörnbrack et al. (2002).

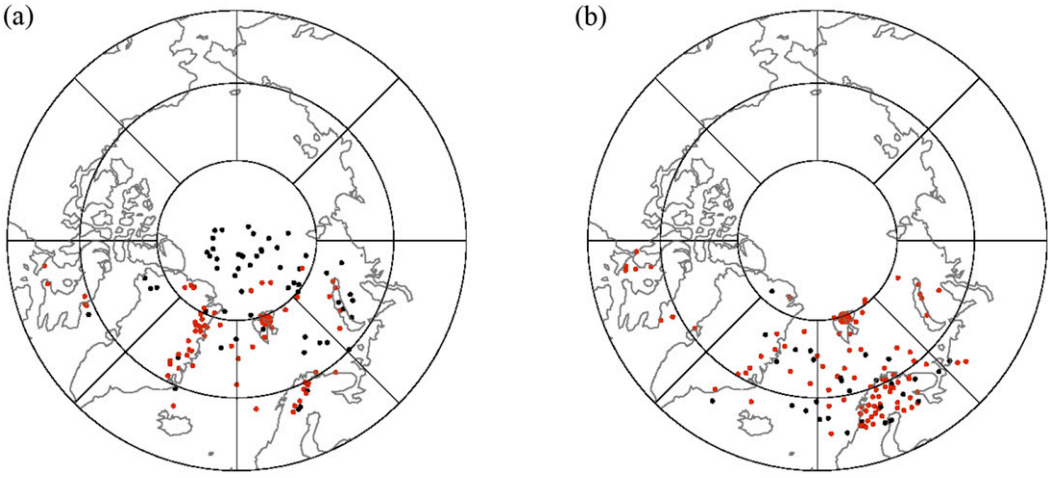

FIG. 9. Locations of the polar cap minimum temperatures T_{MIN} at (a) 30 and (b) 50 hPa from 6-hourly ECMWF IFS cycle 41r2 analyses for December 2015. The red dots mark T_{MIN} values where the absolute value of the horizontal divergence is larger than $2 \times 10^{-4}\,s^{-1}$. The large red dot is the location of T_{MIN} at 0600 UTC 30 Dec 2015.

The effect of mesoscale temperature fluctuations on the polar cap minimum temperatures T_{MIN} at 50 hPa is illustrated by the new IFS cycle 41r2. Figure 3 contains two T_{MIN} curves for a period of 3 months when the new IFS cycle was not yet operational. The red line depicts the former IFS cycle 41r1 with 16-km horizontal resolution and the shorter black line is T_{MIN} of the new, updated operational cycle 41r2 with 8-km horizontal resolution. After 8 March 2016, IFS cycle 41r2 became operational and continues as red line. Obviously, the higher-resolution IFS run achieved much lower T_{MIN} in certain periods, especially at the end of December 2015 and at the end of January 2016 when deviations of up to 7 K occurred. These stratospheric temperature minima were primarily generated by mesoscale gravity waves at various places in the Arctic, especially over Greenland and Scandinavia as shown in Fig. 9 for December 2015. Gravity wave activity was identified by values of the horizontal divergence being larger than $2 \times 10^{-4}\,s^{-1}$ as suggested by Dörnbrack et al. (2012) and Khaykin et al. (2015).

3. Conclusions

The uniqueness of this contribution to the ''picture of the month'' is not only justified by the unusual meteorological situation in the Arctic in midwinter, but also by the coexistence of tropospheric clouds (i.e., cirrus clouds attached to a 12-km high and sharp tropopause) and different types of PSCs between 18- and 28-km altitude over a limited area poleward of 80°N. Synoptic-scale lifting was responsible for formation of the ice clouds near the tropopause and NAT or STS PSCs in the stratosphere. The total large-scale ascent was also associated with the formation of an ozone minihole observed by OMI[2], which was generally aligned with the tropospheric ridge as shown in Fig. 3 [see e.g., Peters et al. (1995) for dynamical aspects of ozone minihole formation]. Adiabatic cooling in the ascending branches of mesoscale mountain waves dropped the stratospheric temperatures far below the threshold temperature for the existence of ice PSCs. The simultaneous formation of synoptic- and mesoscale PSCs inside the Arctic stratospheric vortex happened during a rare meteorological situation during the Northern Hemisphere midwinter. Moreover, it is the remarkable agreement of the simulated wave structure in the IFS short-term forecast and the spaceborne observations, which indicates a significant trend that the finer resolution and increasing realism of operational NWP model outputs offers a valuable quantitative source for mesoscale flow components, which were hitherto not accessible globally (Bauer et al. 2015).

Acknowledgments. Part of this research was funded by the German research initiative ''Role of the Middle Atmosphere in Climate (ROMIC)'' funded by the German Ministry of Research and Education in the project ''Investigation of the life cycle of gravity waves (GW-LCYCLE, 01LG1206A).'' The research of Sonja Gisinger was support by the research group ''Multiscale dynamics of gravity waves (MS-GWaves)'' in the project ''Modification of gravity waves propagating across the tropopause (GW-TP, DO 1020/9-1).'' Access to the ECMWF data was possible through the special project

[2] http://ozonewatch.gsfc.nasa.gov/Scripts/big_image.php?date=2015-12-31&hem=N.

"HALO Mission Support System." The presented radiosonde data were obtained at the AWIPEV research base at Ny-Ålesund, Svalbard. They are part of the Global Climate Observing Systems (GCOS) Reference Upper-Air Network (GRUAN), available via the webpage www.gruan.org. Also, the very constructive comments of three anonymous reviewers helped considerably to improve the paper. The contributions of Michael Pitts and Lamont Poole were supported by the NASA *CALIPSO/CloudSat* Science Team.

APPENDIX

Numerical Weather Prediction Model Data

Operational analyses of the Integrated Forecast System (IFS) of the European Centre for Medium-Range Weather Forecasts (ECMWF) are used to provide meteorological data to characterize the atmospheric situation. The operational analyses and forecasts of the deterministic high-resolution (HRES) IFS cycle 41r2 have a horizontal resolution of about 8 km (T_C1279) and 137 vertical levels (L137).[A1] The model top is located at 0.01 hPa. The enhanced horizontal resolution was achieved by changing from linear (T_L) to cubic (T_C) spectral truncation and introducing an octahedral reduced Gaussian grid. With the cubic spectral truncation the shortest resolved wave is represented by four rather than two grid points and the octahedral grid is globally more uniform than the previously used reduced Gaussian grid (Malardel and Wedi 2016). In December 2015, the IFS cycle 41r2 was not yet in its operational mode but products were disseminated among the users. So, we were able to retrieve forecasts and analysis fields for the current contribution.

CALIPSO *data*

The primary instrument on *CALIPSO* is a lidar or Cloud–Aerosol Lidar with Orthogonal Polarization (CALIOP) that measures backscatter at wavelengths of 1064 and 532 nm, with the 532-nm signal separated into orthogonal polarization components parallel and perpendicular to the polarization plane of the outgoing laser beam. A description of CALIOP and its on-orbit performance can be found in Hunt et al. (2009), and details on calibration of the CALIOP data are provided by Powell et al. (2009). CALIOP has proven to be an excellent system for observing PSCs (Pitts et al. 2007, 2009, 2011, 2013).

[A1] https://software.ecmwf.int/wiki/display/FCST/Implementation+of+IFS+cycle+41r2 and http://www.ecmwf.int/en/about/media-centre/news/2016/new-forecast-model-cycle-brings-highest-ever-resolution.

REFERENCES

Backhouse, W., 1885: Iridescent clouds. *Nature*, **31**, 192–193, doi:10.1038/031192d0.

Bauer, P., A. Thorpe, and G. Brunet, 2015: The quiet revolution of numerical weather prediction. *Nature*, **525**, 47–55, doi:10.1038/nature14956.

Browell, E. V., and Coauthors, 1990: Airborne lidar observations in the wintertime Arctic stratosphere: Polar stratospheric clouds. *Geophys. Res. Lett.*, **17**, 385–388, doi:10.1029/GL017i004p00385.

Carslaw, K. S., and Coauthors, 1998: Increased stratospheric ozone depletion due to mountain-induced atmospheric waves. *Nature*, **391**, 675–678, doi:10.1038/35589.

Dee, D., and Coauthors, 2011: The ERA-Interim reanalysis: Configuration and performance of the data assimilation system. *Quart. J. Roy. Meteor. Soc.*, **137**, 553–597, doi:10.1002/qj.828.

Di Liberto, L., F. Cairo, F. Fierli, G. Di Donfrancesco, M. Viterbini, T. Deshler, and M. Snels, 2014: Observation of polar stratospheric clouds over McMurdo (77.85°S, 166.67°E) (2006–2010). *J. Geophys. Res. Atmos.*, **119**, 5528–5541, doi:10.1002/2013JD019892.

Dörnbrack, A., M. Leutbecher, H. Volkert, and M. Wirth, 1998: Mesoscale forecasts of stratospheric mountain waves. *Meteor. Appl.*, **5**, 117–126, doi:10.1017/S1350482798000802.

——, T. Birner, A. Fix, H. Flentje, A. Meister, H. Schmid, E. V. Browell, and M. J. Mahoney, 2002: Evidence for inertia gravity waves forming polar stratospheric clouds over Scandinavia. *J. Geophys. Res.*, **107**, 8287, doi:10.1029/2001JD000452.

——, M. C. Pitts, L. R. Poole, Y. J. Orsolini, K. Nishii, and H. Nakamura, 2012: The 2009–2010 Arctic stratospheric winter—General evolution, mountain waves and predictability of an operational weather forecast model. *Atmos. Chem. Phys.*, **12**, 3659–3675, doi:10.5194/acp-12-3659-2012.

Dye, J. E., and Coauthors, 1996: In-situ observations of an Antarctic polar stratospheric cloud: Similarities with Arctic observations. *Geophys. Res. Lett.*, **23**, 1913–1916, doi:10.1029/96GL01812.

Eckermann, S. D., and R. A. Vincent, 1989: Falling sphere observations of anisotropic gravity wave motions in the upper stratosphere over Australia. *Pure Appl. Geophys.*, **130**, 509–532, doi:10.1007/BF00874472.

——, A. Dörnbrack, H. Flentje, S. B. Vosper, M. J. Mahoney, T. P. Bui, and K. S. Carslaw, 2006: Mountain wave–induced polar stratospheric cloud forecasts for aircraft science flights during SOLVE/THESEO 2000. *Wea. Forecasting*, **21**, 42–68, doi:10.1175/WAF901.1.

Fritts, D. C., and Coauthors, 2016: The Deep Propagating Gravity Wave Experiment (DEEPWAVE): An airborne and ground-based exploration of gravity wave propagation and effects from their sources throughout the lower and middle atmosphere. *Bull. Amer. Meteor. Soc.*, **97**, 425–453, doi:10.1175/BAMS-D-14-00269.1.

Geelmuyden, H., 1885: Iridescent clouds. *Nature*, **31**, 264, doi:10.1038/031264c0.

Gill, A. E., 1982: *Atmosphere–Ocean Dynamics*. Academic Press, 662 pp.

Hólm, E., R. Forbes, S. Lang, L. Magnusson, and S. Malardel, 2016: New model cycle brings higher resolution. *ECMWF Newsletter*, No. 147, ECMWF, Reading, United Kingdom, 14–19. [Available online at http://www.ecmwf.int/sites/default/files/elibrary/2016/16299-newsletter-no147-spring-2016.pdf.]

Hu, J., R. Ren, and H. Xu, 2014: Occurrence of winter stratospheric sudden warming events and the seasonal timing of spring stratospheric final warming. *J. Atmos. Sci.*, **71**, 2319–2334, doi:10.1175/JAS-D-13-0349.1.

Hunt, W. H., D. M. Winker, M. A. Vaughan, K. A. Powell, P. L. Lucker, and C. Weimer, 2009: *CALIPSO* lidar description and performance assessment. *J. Atmos. Oceanic Technol.*, **26**, 1214–1228, doi:10.1175/2009JTECHA1223.1.

Khaykin, S. M., A. Hauchecorne, N. Mzé, and P. Keckhut, 2015: Seasonal variation of gravity wave activity at midlatitudes from 7 years of COSMIC GPS and Rayleigh lidar temperature observations. *Geophys. Res. Lett.*, **42**, 1251–1258, doi:10.1002/2014GL062891.

Malardel, S., and N. P. Wedi, 2016: How does subgrid-scale parametrization influence nonlinear spectral energy fluxes in global NWP models? *J. Geophys. Res. Atmos.*, **121**, 5395–5410, doi:10.1002/2015JD023970.

Manney, G. L., and Z. D. Lawrence, 2016: The major stratospheric final warming in 2016: Dispersal of vortex air and termination of Arctic chemical ozone loss. *Atmos. Chem. Phys.*, **16**, 15 371–15 396, doi:10.5194/acp-16-15371-2016.

Matthias, V., A. Dörnbrack, and G. Stober, 2016: The extraordinarily strong and cold polar vortex in the early northern winter 2015/2016. *Geophys. Res. Lett.*, **43**, 12 287–12 294, doi:10.1002/2016GL071676.

Maturilli, M., and A. Dörnbrack, 2006: Polar stratospheric ice cloud above Spitsbergen. *J. Geophys. Res.*, **111**, D18210, doi:10.1029/2005JD006967.

Mohn, H., 1893: Irisirende Wolken. *Meteor. Z.*, **11**, 81–97.

Murphy, D. J., S. P. Alexander, A. R. Klekociuk, P. T. Love, and R. A. Vincent, 2014: Radiosonde observations of gravity waves in the lower stratosphere over Davis, Antarctica. *J. Geophys. Res. Atmos.*, **119**, 11 973–11 996, doi:10.1002/2014JD022448.

Nappo, C. J., 2012: *An Introduction to Atmospheric Gravity Waves*. 2nd ed. Academic Press, 400 pp.

Peter, T., 1997: Microphysics and heterogeneous chemistry of polar stratospheric clouds. *Annu. Rev. Phys. Chem.*, **48**, 785–822, doi:10.1146/annurev.physchem.48.1.785.

Peters, D., J. Egger, and G. Entzian, 1995: Dynamical aspects of ozone mini-hole formation. *Meteor. Atmos. Phys.*, **55**, 205–214, doi:10.1007/BF01029827.

Pitts, M. C., L. W. Thomason, L. R. Poole, and D. M. Winker, 2007: Characterization of polar stratospheric clouds with spaceborne lidar: CALIPSO and the 2006 Antarctic season. *Atmos. Chem. Phys.*, **7**, 5207–5228, doi:10.5194/acp-7-5207-2007.

——, L. R. Poole, and L. W. Thomason, 2009: CALIPSO polar stratospheric cloud observations: Second-generation detection algorithm and composition discrimination. *Atmos. Chem. Phys.*, **9**, 7577–7589, doi:10.5194/acp-9-7577-2009.

——, ——, A. Dörnbrack, and L. W. Thomason, 2011: The 2009–2010 Arctic polar stratospheric cloud season: A CALIPSO perspective. *Atmos. Chem. Phys.*, **11**, 2161–2177, doi:10.5194/acp-11-2161-2011.

——, ——, A. Lambert, and L. W. Thomason, 2013: An assessment of CALIOP polar stratospheric cloud composition classification. *Atmos. Chem. Phys.*, **13**, 2975–2988, doi:10.5194/acp-13-2975-2013.

Powell, K. A., and Coauthors, 2009: CALIPSO lidar calibration algorithms. Part I: Nighttime 532-nm parallel channel and 532-nm perpendicular channel. *J. Atmos. Oceanic Technol.*, **26**, 2015–2033, doi:10.1175/2009JTECHA1242.1.

Reichardt, J., A. Dörnbrack, S. Reichardt, P. Yang, and T. J. McGee, 2004: Mountain wave PSC dynamics and microphysics from ground-based lidar measurements and meteorological modeling. *Atmos. Chem. Phys.*, **4**, 1149–1165, doi:10.5194/acp-4-1149-2004.

——, and Coauthors, 2015: Mother-of-pearl cloud particle size and composition from aircraft-based photography of coloration and lidar measurements. *Appl. Opt.*, **54**, B140–B153, doi:10.1364/AO.54.00B140.

Rosen, J. M., N. T. Kjome, V. U. Khattatov, V. V. Rudakov, and V. A. Yushkov, 1992: Observations of ozone and polar stratospheric clouds at Heiss Island during winter 1988–1989. *J. Geophys. Res.*, **97**, 8099–8104, doi:10.1029/91JD02524.

Solomon, S., 1999: Stratospheric ozone depletion: A review of concepts and history. *Rev. Geophys.*, **37**, 275–316, doi:10.1029/1999RG900008.

Stanford, J. L., and J. S. Davies, 1974: A century of stratospheric cloud reports: 1870–1972. *Bull. Amer. Meteor. Soc.*, **55**, 213–219, doi:10.1175/1520-0477(1974)055<0213:ACOSCR>2.0.CO;2.

Störmer, C., 1929: Remarkable clouds at high altitudes. *Nature*, **123**, 940–941.

——, 1931: Höhe und Farbverteilung der Perlmutterwolken (Height and color distribution of mother-of-pearl clouds). *Geofys. Publ.*, **IX**, 3–25.

Strawa, A. W., K. Drdla, M. Fromm, R. F. Pueschel, K. W. Hoppel, E. V. Browell, P. Hamill, and D. P. Dempsey, 2002: Discriminating Types Ia and Ib polar stratospheric clouds in POAM satellite data. *J. Geophys. Res.*, **107**, 8291, doi:10.1029/2001JD000458.

Teitelbaum, H., and R. Sadourny, 1998: The role of planetary waves in the formation of polar stratospheric clouds. *Tellus*, **50A**, 302–312, doi:10.1034/j.1600-0870.1998.t01-2-00004.x.